Express Polymer Letters Vol.18, No.6 (2024) 656–672
Available online at www.expresspolymlett.com
https://doi.org/10.3144/expresspolymlett.2024.48

Research article

Biodegradable scaffold: integration of polylactic acid, hydroxyapatite, and graphene oxide via FDM 3D printing

André da Silva Siqueira[1], *Natália Ferreira Braga*[1,2], *Pablo Andrés Riveros Muñoz*[2,3], *Lucas Freitas de Freitas*[2,4], *Aryel Heitor Ferreira*[2,4,5], *Guilhermino José Macêdo Fechine*[1,2*]

[1]School of Engineering, Mackenzie Presbyterian University, Rua da Consolação, 930, CEP 01302-907 São Paulo, Brazil
[2]Mackenzie Institute for Research in Graphene and Nanotechnologies – MackGraphe, Rua da Consolação, 896, CEP 01302-907, São Paulo, Brazil
[3]Faculdades Oswaldo Cruz, R. Brg. Galvão, 540, CEP 01151-000, São Paulo, Brazil
[4]Instituto de Pesquisas Energéticas e Nucleares, IPEN-CNEN/SP, Av. Lineu Prestes 2242, 05508-000 São Paulo, Brazil
[5] Mackenzie Evangelical College of Paraná – Mackenzie Presbyterian University, 80730-000 Curitiba, Brazil

Received 23 February 2024; accepted in revised form 3 April 2024

Abstract. Extensive research and practical applications have been conducted within the biomaterials domain, focusing on polylactic acid (PLA) based composite. These composites have been explored for their favorable attributes, such as excellent processability, biodegradability, and bioactivity properties, but still lack mechanical properties. In this work, PLA-based nanocomposites were prepared by incorporating hydroxyapatite (HA) and graphene oxide (GO) via melt mixing (extruder). Filaments were obtained to develop scaffolds through 3D printing, utilizing the fused deposition method (FDM). The GO was produced using Hummer's method and characterized by X-ray diffraction (XRD), thermogravimetric analysis (TGA), and Raman Spectroscopy. The composites were analyzed using Fourier-transform infrared spectroscopy (FTIR), molecular weight, contact angle measurements, and thermal, mechanical, and rheological analysis. Adding only 0.05 wt% of GO to both PLA and PLA/HA resulted in enhancements in mechanical properties, particularly tensile strength, and significantly modified the surface properties of the materials studied. Specifically, formulation involving PLA/HA/GO was the only one to exhibit rheological properties compatible with the scaffold production process via FDM. These specific formulations were also investigated regarding cytotoxicity, and the presence of GO induces good cytocompatibility in mouse osteoblast cells (MC3T3). These results suggest that FDM technology can be used to fabricate higher-performance (mechanical and biological) scaffolds for tissue engineering.

Keywords: *polylactic acid, hydroxyapatite, graphene oxide, fused deposition modeling, scaffold*

1. Introduction

In recent years, bone issues have become more prevalent for numerous reasons, such as fractures, disease, cancer, etc. In that regard, the development of scaffolds has been widely studied in the biomedical field as a treatment strategy to overcome tissue regeneration problems. A scaffold is a mechanical structure that aims to support cell proliferation to generate new tissue [1, 2]. The scaffold should mimic the structure of an extracellular matrix. Moreover, the main requirements for manufacturing scaffolds are biocompatibility, mechanical strength, high porosity, and biodegradability [2].

There are many additive manufacturing (AM) techniques for scaffold fabrication, such as stereolithography (SLA), selective laser sintering (SLS) and fused deposition modeling (FDM) [3]; between them, the FDM is a technique of prototyping capable of using thermoplastics materials for 3D printing (3DP) [4], with the advantage of being a simple and fast

*Corresponding author, e-mail: guilherminojmf@mackenzie.br

process with high productivity [3] Furthermore, FDM permits the production of a 3D elaborate parts with many details and adaptable shapes [5] by the deposition of a thin layer of the material producing the part. Many biodegradable materials can be used to produce scaffolds by the FDM process, such as polycaprolactone (PCL) [6], polylactic acid (PLA) [7, 8], poly(hydroxyalkanoates) (PHAs) as poly-3-hydroxybutyrate-*co*-3-hydroxyvalerate (PHBV) [9], and its blends [10]. One of the most promising biopolymers used for biomedical applications is the PLA. Being both biocompatible and biodegradable, this polymer permits its use in the human body [11, 12]. However, PLA has many limitations, such as slow biodegradation rates, poor mechanical ductility, and thermal stability [12]. So, alone, it cannot require all the properties needed for this accomplishment. Incorporating osteoconductive fillers, such as hydroxyapatite (HA), is a valuable way to improve clinical performance due to its similar composition to bones and teeth [13]. The introduction of HA into the PLA matrix neutralizes the PLA's degraded acid products and increases the implant osteoconductivity, thus improving tissue compatibility [14]. Many authors have studied the introduction of HA in PLA [8, 15–19]. Backes *et al*. [15] used the AM to prepare composites of PLA/HA and found an improvement of 12% in the thermomechanical properties of PLA with the addition of 10 wt% of HA; also, the authors observed a slight enhancement in cell proliferation test. Introducing a carbon filler can provide better mechanical properties and extra functional features; consequently, the PLA matrix can be restored even in the presence of HA. Graphene and its derivatives have been at the vanguard of technological applications, and it has been used as a nanofiller to reinforce several polymer matrices [20, 21]. Graphene oxide (GO) has also been extensively explored in the biomedical field due to its cytocompatibility, antibacterial properties, and excellent flexibility [22, 23]. Gong *et al.* [24] studied the composite PLA/HA/GO properties produced by solution blending and casting methods. With the increase of GO content, the tensile strength of PLA/HA/GO composites is enhanced, and this behavior can be assigned to the increase in hardness of PLA/HA/GO composites aroused by the rise of GO addition content with extraordinary mechanical properties. Other publications have also prepared PLA/HA/GO composites [25, 26] but always using a solvent mix strategy that is not environmentally friendly. Only one publication focused on producing a biocompatible nanocomposite based on HA and GO with a polymer matrix using a melt mixing strategy; instead of PLA, the poly(ε-caprolactone) – PCL was used [27]. Based on this prior knowledge acquired by our research group, we will develop a biocompatible nanocomposite with adequate characteristics to produce scaffolds via FDM.

This work aimed to investigate the properties of PLA/HA composites with a fixed amount of 30 wt% of HA, with the addition of different concentrations (0.05, 0.1, and 0.3 wt%) of GO to obtain scaffolds produced by FDM 3D printing. To achieve this goal, the GO and HA were incorporated into the PLA matrix using a melt mix strategy with a twin-screw extruder. After the blending step, the filament was produced by in-house equipment coupled to a single-screw extruder. The scaffolds were prepared by 3DP using the most suitable compositions that managed to make the filaments. The graphite and graphite oxide (GrO) were analyzed by their structure to confirm the oxidation process. The PLA/HA, PLA/GO, and PLA/HA/GO composites were characterized by Fourier-transform infrared spectroscopy (FTIR), Raman, molecular weight (Size Exclusion Chromatography), contact angle, Differential scanning calorimetry (DSC) and mechanical tensile tests. The rheological tests were conducted to verify which compositions could be used in the filament-produced process. The scaffolds were prepared, and vitro cytotoxicity was subsequently evaluated for cytocompatibility assessment.

2. Experimental

2.1. Materials

Polylactic acid (PLA) (INGEO Biopolymer from Natureworks LLC – grade 3251D, Plymouth, United States) with molecular weight (M_w) 96 000 g/mol, melt flow index (MFI) of 35 g/10 min and density of 1.24 g/cm^3. Hydroxyapatite (HA) powder (purity: 99%; diameter: 20–40 nm) supplied from Sigma-Aldrich (MilliporeSigma – Burlington, United States). Graphite in powder with 99.9% purity from Sigma-Aldrich (MilliporeSigma - Burlington, United States). Dulbecco's Modified Eagle's Medium (DMEM, GIBCO) from Thermo Fisher Scientific (Waltham, United States). Fetal bovine serum (FBS), Penicillin-Streptomycin, Dimethylsulfoxide (DMSO), DAPI (fluorescent dye for nuclei), and formaldehyde

from Sigma-Aldrich (MilliporeSigma – Burlington, United States). XTT assay kit from Abcam® (Cambridge, UK).

2.2. Graphite oxidation

The graphite oxidation was firstly done by adding 1 g of graphite and 60 mL of sulfuric acid (VETEC – Duque de Caxias, Brazil) in a 500 mL volumetric flask (previously placed in an ice bath) and kept under stirring conditions for 15 min. After this, 100 mL of a solution of $KMnO_4$ (Sigma-Aldrich – Burlington, United States) 35 mg/L was slowly added to the mixture using a peristaltic pump at a 6.8 mL/min flow rate. This system was maintained for 5 min in an ice bath. This mixture was stirred for 2 h in an ice bath and then diluted with 100 mL of water. To remove the excess oxidizing agent, 0.5 mL of aqueous hydrogen peroxide (H_2O_2 – 30% from VETEC – Duque de Caxias, Brazil) solution was slowly dropped until the system stopped bubbling and stirred for 5 min. The system was kept at rest for 24 h. After this period, the supernatant was removed. The precipitated was filtered and washed with 500 mL of deionized water and then with 250 mL of a 10% aqueous hydrochloric acid (HCl 37% –VETEC – Duque de Caxias, Brazil) solution to remove sulfate ions, 250 mL of ethanol to remove organic contaminants and then washed with additional 200 mL of deionized water. The material was placed in a vacuum oven at 60 °C for 24 h, which is the graphite oxide (GrO).

2.3. GrO exfoliation

Initially, 240 mg of GrO was added to an amber flask, along with 480 mL of ethyl alcohol (99.8% from Synth – Brazil), and placed in an ultrasound bath (Elmasonic – Germany) in sweep mode with a frequency of 37 Hz at 30 °C for 120 min. Thus, a dispersion of GO of 0.5 mg/mL in ethanol was obtained and maintained by magnetic solid stirring for 12 h to further use in the solid-solid deposition process to prepare the composites.

2.4. Composites preparation

Initially, PLA pellets were immersed in liquid nitrogen for 20 min and ground using a knife mill machine (SOLAB SL 31 – Brazil). Then, the powder was sieved in a 30 mesh mechanical sieve shaker. As described in the literature, the solid-solid deposition technique (SSD) was applied to perform a homogeneous mechanical deposition of the GO on top of the polymer granules [28]. This method uses a rotary evaporator to deposit the exfoliated GO on the surface of the polymer powder while the exfoliation medium (water) is evaporated. The main differentiating factor of this strategy is that it allows the exfoliated nanomaterial to be deposited over the polymer granules' surface without them restacking to a bulky state. The PLA/HA/GO was made the same way, adding the HA in the fixed concentration of 30% with the PLA powder and GO suspension, and the PLA/HA mixture was made directly in the extrusion without using the SSD technique.

After that, the materials were vacuum oven dried at 100 °C for eight h and extruded using a co-rotating twin screw extruder (Thermo Fisher Scientific U.S. – Process 11, $L/D = 40$). The feed was 4 g/min, and the screw speed was held constant at 100 rpm. The temperature profile was 180, 190, 190, 185, 185, 190, 190, and 185 °C from the feed section to the die. The circular cross-section of the matrix used was 2 mm in diameter. The filaments were produced by a system coupled to the end of the extruder with pull speed control, keeping the filament diameter around 1.75 mm. The extrudate was cooled using an air-cooled conveyor belt, and the material in the form of a filament was wound onto a reel. Table 1 shows all formulations obtained. Based on a previous study, 30 wt% of HA was used in all compositions [29].

2.5. Graphite and GrO characterization

To characterize the graphite materials, Raman scattering analysis, X-ray diffraction (XRD), and Thermogravimetric analysis (TGA) were performed.

The Raman spectra were carried out with a Witec UHTS 300 (Germany) spectrometer coupled to a 50× resolution optical microscope using a laser with a wavelength of 532 nm.

Table 1. Composites formulation in wt%.

Sample	PLA [wt%]	HA [wt%]	GO [wt%])
PLA	100.00	–	–
PLA/GO-0.05	99.95	–	0.05
PLA/GO-0.1	99.90	–	0.10
PLA/GO-0.3	99.70	–	0.30
PLA/HA	70.00	30	–
PLA/HA/GO-0.05	69.95	30	0.05
PLA/HA/GO-0.1	69.90	30	0.10
PLA/HA/GO-0.3	69.70	30	0.30

The samples' crystalline structure analyses were performed by X-ray diffraction in a Rigaku Miniflex II (Tokyo, Japan) diffractometer with a Cu-tube (Cu K_α = 0.15418 nm) at a 5°/min scanning rate over a range from 5° to 60°.

The thermal properties of the materials were measured on a thermogravimetric analyzer STD Q600 of TA instruments (New Castle, U.S.) under a nitrogen atmosphere (40 mL/min) from 30 to 700 °C at a heating rate of 10 °C/min, held for 5 min and cooled down to room temperature.

2.6. HA characterization

HA was characterized by Raman and XRD in the same conditions as GrO, described above. The HA was also characterized by Fourier transform infrared spectroscopy (FTIR) using a Shimadzu (Kyoto, Japan) Spectrophotometer, IRAffinity-1, using accessory Attenuated total reflectance (ATR) with ZnSe crystal. The spectra were recorded within a range of 4000–500 cm^{-1}.

2.7. PLA/GO and PLA/HA/GO composites characterization

Raman spectroscopy

For the Raman analysis of the composites, films were prepared, approximately 120 µm thick, by hot press (Solab SL12/20 –- Brazil) at 190 °C, 1.2 tons for 1 min. A Witec UHTS 300 (Germany) spectrometer was used, coupled to a 50× resolution optical microscope, using a laser with a wavelength of 532 nm.

FTIR-ATR (Fourier-transform infrared spectroscopy in attenuated total reflectance)

The polymeric films were also used for the FTIR-ATR analysis, using a Cary 630 FTIR of Agilent Technologies (Santa Clara, U.S.) with 64 scans for each composition, 4 cm^{-1} of resolution and a measurement range of 500 and 4000 cm^{-1}.

Size exclusion chromatography

For the determination of the number average molecular weight ($\bar{M}_n$), Weight average molecular weight ($\bar{M}_w$) and polydispersity ($\bar{M}_n/\bar{M}_w$) of pristine PLA and the composites, size exclusion chromatography (SEC) was performed. About 60 mg of each composite was dissolved in 20 mL chloroform (Clorosolv Plus for HPLC from Sigma-Aldrich – U.S.) into a 40 mL vial and put in stirring for 30 min, then filtered on a nanoporous filter (Millipore) for removing the fillers. The SEC was performed on a Viscotec (Germany) 430 chromatograph (GPC-HT 350) with a refractive index detector. The column set consisted of a guard column and a combination of three separation columns (K-806M, Shodex), with 1 mL/min flow, where the eluent solvent used was Tetrahydrofuran (THF, Sigma Aldrich – U.S.). Each run was performed 60 and 10 min post-running, and the injection volume was 100 mL.

Mechanical properties

Tensile strength tests were performed according to ASTM D638 to evaluate the mechanical properties using a type IV specimen. The extruded filament was granulated, and the pellets obtained were processed in a Plastic Injection Molding Machine model Haake Minijet Pro (Thermo Scientific – U.S.). The specimens were produced with a barrel temperature of 190 °C, 200 bar of injection pressure, 100 bar of holding pressure, and a mold temperature of 60 °C. The specimens were stood for 48 h at room temperature for stabilization and then dried for 12 h in a vacuum oven.

A tensile test was performed on at least eight specimens of each composite in a universal electromechanical testing machine (Instron 3369 – Norwood, U.S.) at 20 °C with a 10 mm/min crosshead speed and a cell load of 10 kN.

Contact angle and surface free energy

The tests were carried out on the specimens obtained for the tensile strength test using a DAS 100B (KRUSS® – Hamburg, Germany) goniometer by the sessile drop method. The solvents were deionized water obtained by the MiliQ® system and Ethylene glycol PA. 5 µL of each solvent were injected. The drops transferred to the surface of the composites were evaluated by the ADVANCE® software, where the angles were obtained.

Besides that, this method allows the calculation of the surface free energy and its polar and dispersive components. The relationship between surface free energy and contact angles is given by Fowkes equation (Equation (1)) [30]:

$$\gamma_L(1+\cos\theta) = 2\left(\gamma_s^d\gamma_L^d\right)^{1/2} + 2\left(\gamma_s^p\gamma_L^p\right)^{1/2} \quad (1)$$

where θ is the contact angle; γ_L is the surface tension of the liquid, and γ_s is the surface free energy. The

terms with the superscript *d* and *p* are the dispersive and polar components of the surface free energy.

Differential scanning calorimetry (DSC)

Approximately 6 mg of sample (removed from the tensile tests specimen) of each composition were sealed in aluminum pans and analyzed using a differential scanning calorimeter DSC 7000X – HITACHI (Chiyoda, Japan). The samples were initially heated from 30 to 200 °C at 10 °C/min and cooled at 10 °C/min to 30 °C. All the measurements were carried out under the nitrogen atmosphere, with a flow rate of 100 mL/s.

It was evaluated transitions temperatures, as glass transition temperature (T_g), melting temperature (T_m) and cold crystallization temperature (T_{cc}). Also, the crystallinity degree of the samples was calculated using the Equation (2):

$$X_c = \frac{\Delta H_m + \Delta H_{cc}}{\omega \cdot \Delta H_m^o} \cdot 100 \quad (2)$$

where ΔH_m and ΔH_{cc} are the melting and cold crystallization enthalpy, respectively, and ω is the weight fraction of PLA in the sample. ΔH_m^o is the heat of fusion corresponding to the enthalpy of 100% crystalline PLA, which is 93.7 J/g [31].

Rheological analysis

The rheological behavior of neat PLA and composites was analyzed using a rheometer ANTON PAAR® (Graz, Austria) model MCR 102, using a 25 mm radius parallel plate geometry with a 1 mm gap. The filament was pelletized and dried in a vacuum oven at 60 °C for 12 h, and the pellets were positioned directly onto the preheated bottom geometry of the equipment for the analysis. All the tests were performed under a nitrogen atmosphere to avoid oxidation.

Three oscillatory tests were carried out: first, the dynamic strain sweep pre-test was conducted at a frequency of 6.8 rad/s to determine the linear viscoelastic regime (LVR). Subsequently, temperature sweep tests were carried out in the oscillatory regime (frequency of 6.8 rad/s) to determine the dynamic properties of the materials. For frequency scanning assays in the frequency sweep test, the temperature was set at 140 °C and 1.0% deformation. Rotational tests were performed to obtain steady-state shear flow in the 0.01 to 100 s^{-1} range.

Processing scaffolds by FDM

The scaffolds were made using FDM 3D printing (Cliever CL PRO – Belo Horizonte, Brazil) consisting of a printing platform with dimensions of 230 mm wide × 230 mm long × 200 mm high, with two extrusion heads. The impressions were made with a 0.4 mm nozzle and a layer resolution of 0.1 mm. The platform was heated to 50 °C, and all printing parameters were controlled by CLIEVER STUDIO® 5.0 software. Figure 1 presents the draw scheme of the scaffolds made with 6 mm in edge, the Gyroid structure.

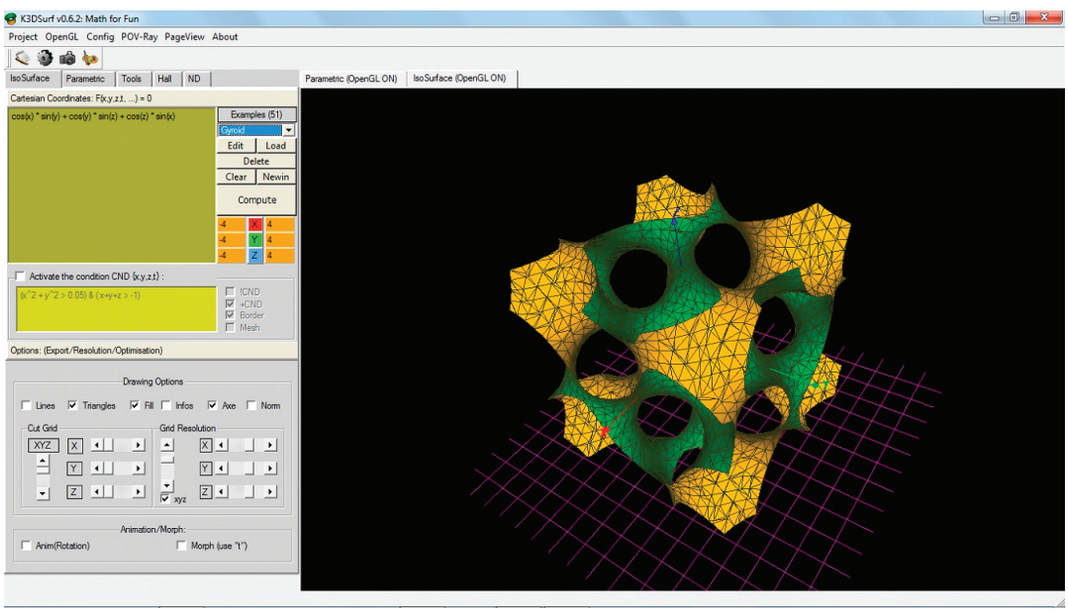

Figure 1. Gyroid structure.

2.8. In vitro biocompatibility

Cytotoxicity test

Before seeding MC3T3 cells (mice osteoblasts) on the scaffolds, an assessment of the cytotoxicity of PLA/HA and PLA/HA/GO material was conducted. The cell viability was tested using the 3D scaffolds (Test by direct contact) and their extracts according to ISO 19993-5 with additional time points. The extracts were obtained by incubating the scaffolds in Dulbecco's Modified Eagle's medium (DMEM, GIBCO) supplemented with 10% fetal bovine serum (FBS), 100 IU/mL penicillin and 100 µg/mL streptomycin for 24, 48 h, or 1 week, at 37 °C. After the incubation periods, the extracts were used in the experiment. MC3T3 cells were seeded in 48 well plates (10^5 cells/well) containing the 3D scaffolds or extracts. After 48 h, the metabolic activity was tested using the XTT assay kit (Abcam®), according to the manufacturer's instructions; the results are expressed in the percentage of cell viability compared to negative controls. Positive controls consisted of cells incubated with 50% dimethylsulfoxide (DMSO).

Cell seeding

MC3T3 cells were seeded on the surface of discs made from the same material as the scaffolds at the density of 10^4 cells and cultured in DMEM medium supplemented with 10% fetal bovine serum (FBS), 100 IU/mL penicillin and 100 µg/mL streptomycin on 96 well plates. This way, the cells would grow on top of the discs, which would be compared with cells grown on the plate substrate (Control cells).

The cells were cultured for 5 days; the discs were removed and placed in cell-free wells so that only the cells growing on the discs contributed to the result. Then, the cell viability was measured using the XTT assay. The results are expressed in the percentage of cell growth compared to control cells. ANOVA one-way with the Tukey test was used to assess statistical significance among the sample means ($p < 0.05$).

Cell visualization on the disc surface

Three discs were used for cell growth and image acquisition: pure PLA, PLA with 0.05% graphene oxide (GO 0.05), and PLA with 0.3% GO, apart from a glass cover slide used as a control for cell growth. All discs had a diameter of 0.5 cm and were placed in 24 well plates on the bottom of each well. $5 \cdot 10^4$ (MC3T3 cells) were seeded on top of them and placed in an incubator for 72 h. Then, the cells were dyed with DAPI (fluorescent dye for nuclei). Finally, the cells were fixed with 4% formaldehyde, and the scaffolds were placed on a glass slide to acquire confocal images.

DAPI was excited with a 405 nm light source, and brightfield images were also taken. However, it is worth mentioning that brightfield images were not always possible as the discs containing graphene oxide were too opaque.

3. Results and discussion

GrO and HA characterization

Figure 2a shows the Raman spectra for the pristine graphite and GrO. Differences in the material's structure can be observed after oxidation. The band at 1572 cm^{-1}, presented in the graphite and GrO, is related to the G-band, which is attributed to the C=C symmetric stretching mode [32]. The band at 2690 cm^{-1} is the 2D-band, which is inherent in the graphitic structure.

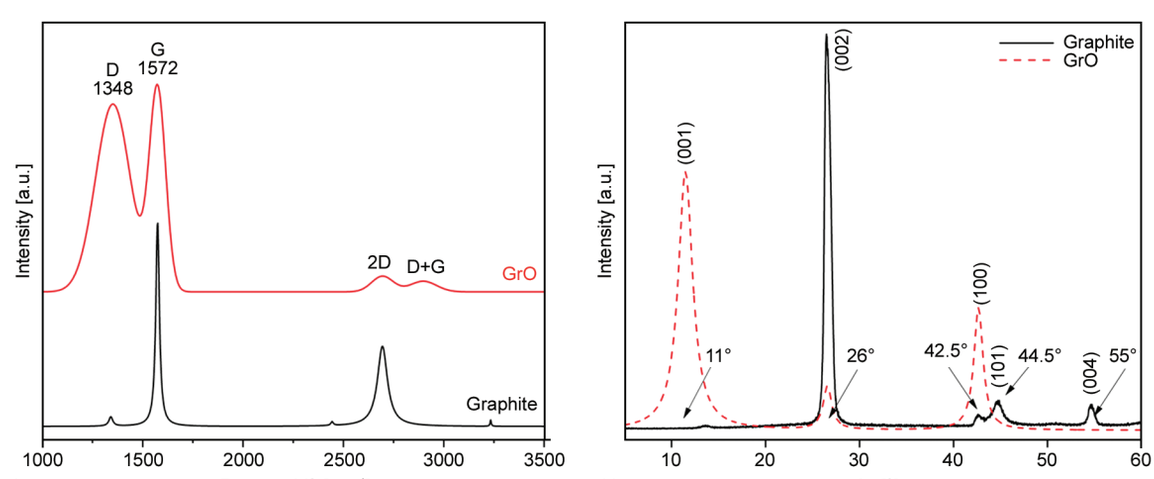

Figure 2. a) Raman spectrum and b) XRD pattern of graphite and GrO.

The D-band at 1348 cm^{-1} is related to sp^3 carbon hybridization due to the defects in the graphitic structure and incomplete bonds at the edges of the graphene sheets. This band is more intense on GrO because the oxidation process induces defects in the material due to the oxidation method allowing oxygen functional groups to be introduced. In the same way, the D+G-band at 2920 cm^{-1} is related to defects of the structure [33].

The intensity ratio between D- and G-bands, I_D/I_G, determines the disorder of the crystal structure of the material [34]. The I_D/I_G of GrO is 0.98, which is significantly higher than the I_D/I_G of graphite (0.08), indicating increasing defects after the oxidation process.

Figure 2b presents the XRD for graphite before and after oxidation. There is an intense and tight peak at 2θ = 26° for graphite, which corresponds to the refraction of the (002) plane, as well as another peak at 2θ = 55° corresponding to the plane (004) [35]. After oxidation, the 2θ = 26° peak decreased its intensity drastically, and a new peak occurred at about 2θ =11°, which evidences the increase of the interplanar spacing in the direction (002) for d_{002} = 0.803 nm. The 2θ = 55° peak has disappeared, thus showing a change in the structure of graphite due to the increase in the distance between layers caused by the oxidation process that produced oxygen functional groups [35, 36].

Figure 3 presents the TGA curves for graphite and GrO. At the temperature range studied, the graphite is very thermally stable and did not show weight loss, indicating the absence of functional groups, which can also be related to the purity of the material. However, in a different behavior, the GrO curve presented three stages of weight loss. First, from 30 to 100 °C, the material lost about 10% in mass, which can be attributed to the loss of water molecules adsorbed [37]. From 100 to 240 °C can be seen in the second stage, when the material lost around 25% in mass, attributed to the remotion of oxygenated groups, evidencing the oxidation process once these groups turn the material more unstable. Finally, at 240 °C, the material loses mass due to pyrolysis.

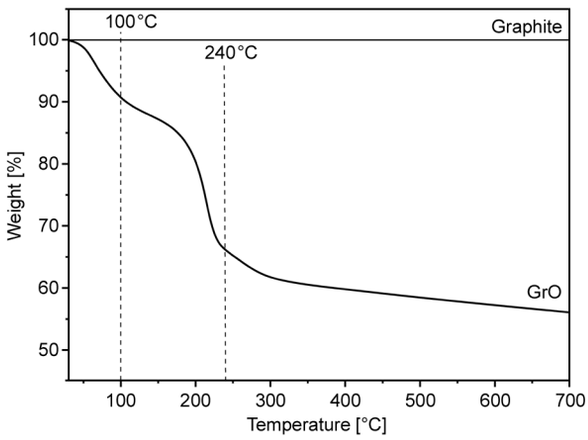

Figure 3. TGA curves of graphite and GrO.

The results of FTIR, Raman and XRD of HA are presented in the Figure 4 respectively. In FTIR spectrum, the bands related are: 1460 cm^{-1}, referring to water absorbed, 1414 cm^{-1}, referent to CO_3^{-2} groups, the intense band at 1022 cm^{-1} which accompanies two less intense bands at 963 and 879 cm^{-1} are related to PO_4^{3-} [38].

In Raman spectrum, the band at 1047 cm^{-1} is from asymmetric stretch mode PO_4^{3-}. The intense band at 964 cm^{-1} is related to the fully symmetrical stretch mode of PO_4^{3-}. The bands at 585 and 433 cm^{-1} are related to the bending mode of the groups HPO_4^{2-} and PO_4^{3-}, respectively [39].

The most critical peaks from XRD are presented at 2θ = 32°, 32.5°, 33°, and 34°, referring respectively to the planes (211), (112), (300), (202) of the crystal structure of HA [39].

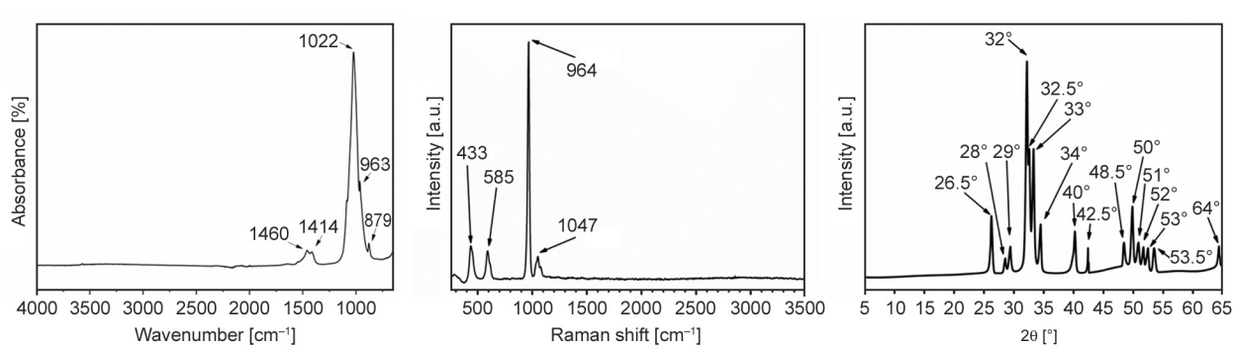

Figure 4. FTIR spectrum (a), Raman spectrum (b), and XRD pattern (c) for HA.

Composites characterization

Regarding the structural chemical changes and interactions between the PLA, HA, and GO that may have happened after processing, FTIR analysis is an important data source, and it is presented in Figure 5a. In FTIR spectra of HA, there is an intense band at ~1022 cm^{-1}, related to PO_4^{3-}, characteristic of this material. There is a band at around 1019 cm^{-1} in the neat PLA spectra. In PLA/HA and PLA/HA/GO composites, an overlap of these two bands occurred, and a broader and more intense band can be observed. Thus, the results confirmed the existence of HA in the PLA/HA composites. Concerning the composites containing GO, the bands related to it coincide with the bands of the PLA. Commonly, the GO presents peaks related to the carboxyl groups ~3400 cm^{-1}, carbonyl (~1720 cm^{-1}), and epoxy (~1240 cm^{-1}) [40]. Also, the PLA/GO and PLA/HA/GO composites present a very low GO content (from 0.05 to 0.3 wt%) compared to HA (30%), making verifying its presence and interaction within the polymer more difficult.

In Raman spectra (Figure 5b) of the composites containing HA, a 960 cm^{-1} band, like that typically identified in the pristine HA (as shown in Figure 4b), can be identified. Therefore, this band can be considered evidence of the presence of HA in the composites. Another inference is that the interaction of HA in composites is strictly physical since its characteristic band was not displaced.

Another band to be noticed, but with low intensity, occurs only in the composites with higher amounts of GO close to 1595 cm^{-1}. This band is attributed to the G-band identified in the GrO before the dispersion and mixing processes (Figure 2a). Still, this band exhibits a displacement of ~20 cm^{-1}, evidencing the occurrence of chemical interactions with the other components of the composite, which may result in a high transferability of GO properties to the composite.

Molecular weight data

The molecular weight can allow the evaluation of the degradation of PLA during the extrusion processing, which may cause scission and crosslink reactions. So, it was compared to the PLA as received (unprocessed PLA before extrusion) and the processed PLA after extrusion. The results of $\bar{M}_n$ and $\bar{M}_w$ are shown in Table 2. Firstly, there was an increase in $\bar{M}_n$ and a reduction in $\bar{M}_w$ of the processed PLA compared to the unprocessed PLA. This change indicates the occurrence of scission reactions in the larger chains because of thermo-oxidative degradation

Table 2. Numerical ($\bar{M}_n$) and weight ($\bar{M}_w$) average molar masses and polydispersity ($\bar{M}_w/\bar{M}_n$) of unprocessed and processed PLA in the presence or absence of HA and/or GO.

Sample	$\bar{M}_n$ [Da]	$\bar{M}_w$ [Da]	$\bar{M}_w/\bar{M}_n$
Unprocessed PLA	44 700	96 600	2.16
PLA	54 100	80 700	1.49
PLA/GO 0.05	50 800	73 900	1.45
PLA/GO 0.1	45 500	74 220	1.63
PLA/GO 0.3	47 200	75 540	1.60
PLA/HA	54 600	83 400	1.53
PLA/HA/GO 0.05	59 700	79 000	1.33
PLA/HA/GO 0.1	58 700	79 400	1.35
PLA/HA/GO 0.3	54 500	77 900	1.43

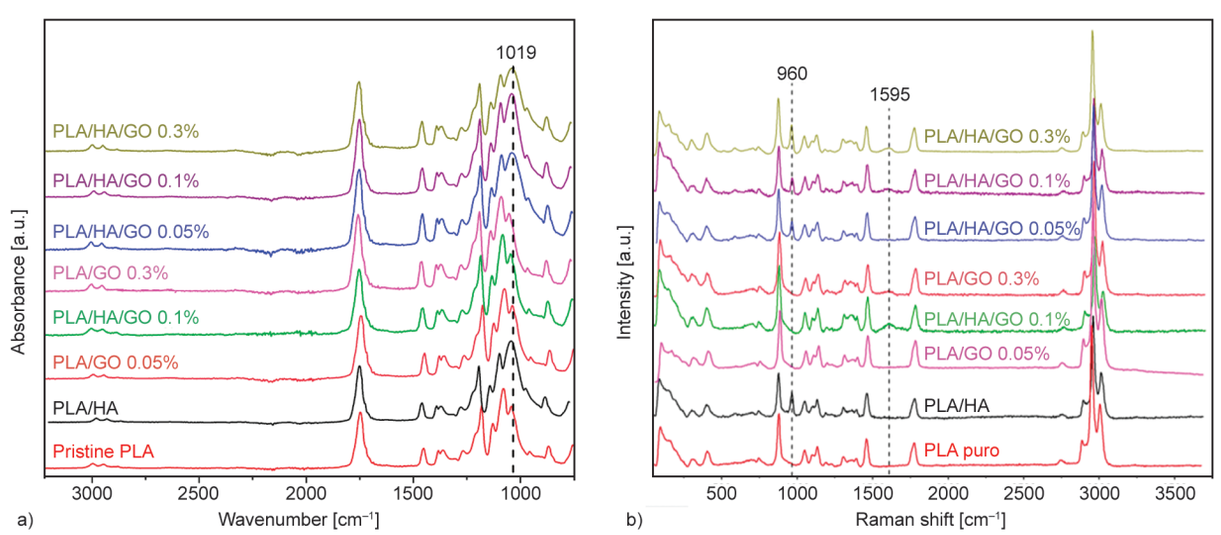

Figure 5. FTIR (a) and Raman (b) are for PLA and composites PLA/GO, PLA/HA, and PLA/HA/GO.

during processing, reducing the $\bar{M}_n$ and increasing the average number of smaller chains. Nonetheless, this increased effect of $\bar{M}_n$ was reduced by the addition of GO, as the presence of water adsorbed on the surface of the GO sheets (even after drying in an oven, adsorbed water remains in the structure) leads to hydrolysis reactions of the polymeric chains of PLA during processing causing a reduction in both in $\bar{M}_n$ and $\bar{M}_w$. This effect worsens with the increase in the concentration of GO. On the other hand, the addition of HA appears to have no degradation reactions, but when combined with GO, a reduction in $\bar{M}_w$ is observed again. It is possible to infer that adsorption on GO can intensify the degradation of water through the PLA chains of hydrolysis mechanisms. For PLA/HA/GO composites, the $\bar{M}_w$ display values close to each other, indicating that the scission chain reactions were very similar for all systems.

In addition, it is worth highlighting that the GO may contain acidic residues from its synthesis process, which catalyze the hydrolysis of PLA. The HA, on the other hand, has basic characteristics that would reduce the effects of the residual acid of GO, leading to a smaller reduction in the $\bar{M}_n$ of the hybrid composites compared to PLA/GO nanocomposites.

Contact angle and surface free energy

Contact angle analysis is an essential technique to obtain information about the surface properties of the materials, as well as their hydrophilic and hydrophobic characteristics. Table 3 presents the results of the contact angle in water and ethylene glycol of PLA and all compositions with HA and/or GO. PLA is a nonpolar polymer with low surface energy, which makes its wettability difficult. In applications such as biomedical, the increase in surface hydrophilicity and reduction in the angle of contact enables cell growth [41]. Studies indicate that the ideal contact angle for cell adhesion is between 60° and 70° between the surface of the bioimplant and the water [42]. With the incorporation of 0.05 wt% of GO, there was a reduction in the contact angle in water, which leads to improved wettability and allows an interaction with aqueous fluids, which helps cell adhesion in biological environments. However, further increasing the concentration of GO, the contact angle returns to higher values, evidencing once again that the efficiency of this property modification occurs in very low GO mass proportions. Probably, as the concentration of GO increases, the particle-particle interactions increase, and the effect on the polymer matrix due to the presence of GO is not as strongly observed. When HA is added to the system, the contact angle also decreases. In the concentration of 0.05 wt% of GO in PLA/HA, the contact angle reached the smallest value (average of 67°); however, this value increased again in the samples with 0.1 wt% (84°) and 0.3 wt% (88°) of GO. Therefore, under the conditions analyzed, the best composition achieved for biomedical application was the PLA/HA/GO 0.05% composite.

Another factor that demonstrates the improvement of the surface properties is the increase, mainly in the polar component of surface energy (Table 3). The neat PLA has a surface energy of approximately 38 mJ/m^2, with meager participation of the polar component, about 1.5 mJ/m^2. The outstanding dispersive contribution in its surface properties is due to the high amount of CH_3 groups, thus determining a great hydrophobic character [43]. When HA is incorporated, the surface energy decreases; however, the polarity increases due to the hydrophilic character of HA [44]. Interactions of the polar groups of HA with the external surface probably occur. The PLA/GO composite showed a similar effect, but a much smaller amount of GO was required to produce

Table 3. Contact angle in water and ethylene glycol and surface energy components for PLA and the composites.

Sample	Contact angle [°]		Energy [mJ/m^2]		
	Water	Ethylene glycol	Surface energy	Dispersive component	Polar component
PLA	99±0.81	65±0.2	38.77±2.41	38.7±2.2	1.44±0.1
PLA/GO 0.05	80±0.7	63±0.73	22.78±1.03	20.92±0.55	9.01±0.87
PLA/GO 0.1	91±2.91	63±3.3	23.26±2.98	21.64±2.3	8.54±1.9
PLA/GO 0.3	94±0.5	65±2.4	23.09±2.38	21.52±1.64	8.38±1.73
PLA/HA	91±3	61±6	24.47±2.6	22.7±2	9.15±2.2
PLA/HA/GO 0.05	68±2.5	62±2.2	35.79±2.32	5±0.3	35.44±2.3
PLA/HA/GO 0.1	75±3	58±6	25.99±2.8	10.08±2	23.96±2.6
PLA/HA/GO 0.3	89±1.1	65±1.5	18.68±2.57	14.15±2.03	12.20±1.57

the same effect as HA. GO also has a hydrophilic character due to the oxygenated groups present on its surface [45]. In the PLA/HA/GO composite, the polar portion increased even more, which demonstrates a synergistic effect of increasing the polarity of the HA and GO fillers.

Thermal analysis

Figure 6 show the DSC curves of the first heating scan for PLA and PLA/GO and PLA/HA/GO composites, respectively. From these curves, it was possible to obtain information such as glass transition temperature (T_g), cold crystallization temperature (T_{cc}), melting temperature (T_m), crystallinity degree (X_c), and cold crystallization and melt enthalpy (ΔH_{cc} and ΔH_m), which are summarized in Table 4.

The T_g of PLA is around 55 °C and the addition of GO or HA increased the T_g, reaching 68 °C in PLA with 30 wt% of HA, indicating that, initially, this filler interfered considerably in the energy needed for the amorphous phase of the PLA to acquire mobility. Also, the addition of GO increased the T_g of PLA.

From the curves of the first heating, it is possible to see that all the samples presented an exothermic peak around 100 °C, corresponding to the cold crystallization temperature (T_{cc}), where the polymer crystallizes during the heating process. With the incorporation of GO or HA, the T_{cc} tends to decrease due to the formation of nucleation centers of PLA crystals promoted by the filler. Similar results can be found in the literature, as reported by some authors [17].

The heating scans indicate that GO alone decreases the T_m values. As mentioned before, with the molecular weight data, GO strongly degrades PLA. As a consequence of the scission reactions that can occur at the lamellar fold surfaces, the crystals' surface free energy increases, and the melting temperature decreases [46].

The X_c of PLA was found at 9.67% and considerably increased to 18.65% with the addition of 30 wt% of HA; thus, the HA acted as a nucleating agent for nuclei formation and crystal growth. Following the same pattern, the X_c of PLA/HA/GO also increased compared to the neat PLA.

Mechanical properties

From the tensile test, it was possible to determine variations in the mechanical behavior of the composites

Table 4. Values of T_g, T_{cc}, ΔH_{cc}, T_m, ΔH_m and X_c, obtained by first heating of DSC.

Sample	T_g [°C]	T_{cc} [°C]	ΔH_{cc} [J/g]	T_m [°C]	ΔH_m [J/g]	X_c [%]
PLA	55	106	29.40	173	38.46	9.67
PLA/GO 0.05	61	104	28.15	172	36.09	8.48
PLA/GO 0.1	59	97	19.10	170	28.49	10.03
PLA/GO 0.3	64	98	12.92	171	18.92	6.42
PLA/HA	68	100	20.17	171	32.27	18.45
PLA/HA/GO 0.05	66	100	23.35	172	36.52	20.09
PLA/HA/GO 0.1	66	100	22.62	173	35.96	20.37
PLA/HA/GO 0.3	63	99	13.40	172	25.67	18.71

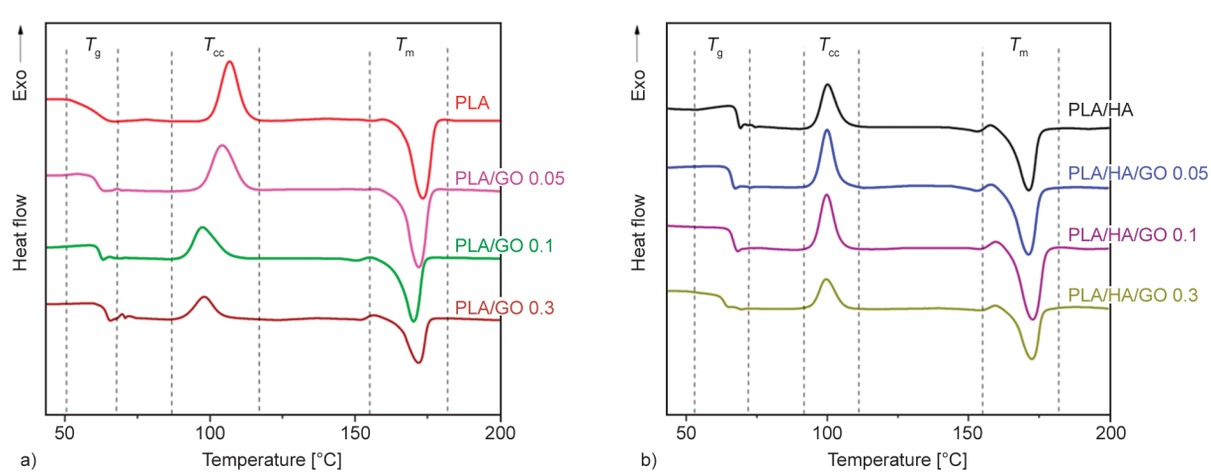

Figure 6. First heating DSC curves of PLA, a) PLA/GO, and b) PLA/HA/GO composites.

compared to neat PLA, such as Young's modulus (*E*), ultimate tensile strength (*UTS*), and elongation at break. The results obtained are summed up in Table 5. The results showed considerable changes in *E* when inserting the fillers in the system: an increase of approximately 20% in *E* could be observed in the composite with 0.05 wt% of GO compared to the neat polymer. This demonstrates a strong interaction between GO and PLA, even in small content, as a large load transfer was applied in the matrix to the dispersed phase. This behavior also evidences the efficiency of GO dispersion in the matrix, as the more dispersed the filler, the better the load transfer to the particulate, proving the excellent performance of GO as filler and the effectiveness of the processing method used [47]. The mechanical properties depend on the crystallinity of PLA, so, by DSC results, the X_c of PLA/GO is 0.3% reduced, and so on the *E*, probably by the formation of aggregates that reduce the interfacial area between polymer and particle. Further, the incorporation of HA in PLA led to a marked enhancement of almost 36% in Young's modulus and a reduction of 31% in elongation at break, compared to the pure PLA. Such high proportions (30 wt%) of HA in the polymeric matrix are typical of agglomerates that can act as stress concentrators in the structure, leading to the material's embrittlement [48]. Additionally, with the addition of 0.05 wt% of GO in PLA/HA, there was an increase of 18% in *E*, reaching the highest value of 5314 MPa; this demonstrates that in these proportions, the GO and HA are acting to improve the material's mechanical performance. However, the same trend in PLA/GO composites reappears in PLA/HA/GO composites, where *E* decreases with increasing GO concentration.

About the *UTS*, there was a reduction in this property with the addition of a more significant amount of GO and even more with the addition of HA. The amount of 0.05 wt% GO does not show any significant variation when compared with neat PLA. The combination of HA and GO also does not affect the ***UTS***. However, it is evident that the GO acted as a recovery filler to overcome the mechanical properties and disadvantages imposed by the presence of HA.

Table 5. Mechanical results obtained by tensile test for PLA, PLA/GO, and PLA/HA/GO composites.

Sample	*E* [MPa]	*UTS* [MPa]	Elongation at break [%]
PLA	3273±143	59±2	1.7±0.1
PLA/GO 0.05	3947±270	58±6	1.9±0.1
PLA/GO 0.1	3457±213	54±4	1.9±0.1
PLA/GO 0.3	3234±910	55±7	1.7±0.2
PLA/HA	4479±244	45±4	1.1±0.1
PLA/HA/GO 0.05	5314±183	47±3	1.2±0.2
PLA/HA/GO 0.1	4123±150	45±3	1.1±0.1
PLA/HA/GO 0.3	3821±434	46±4	1.1±0.2

Rheological analysis

Rheological analyses were carried out to adjust the correct parameters for FDM processing for all types of samples. A commercial PLA (CLIEVER®) was taken as a reference, and it was very used to the FDM process to compare with the neat PLA and composites produced here.

It was found that the liner viscoelastic regime started from 10%. So, all rheological tests were performed at a constant deformation of 12%, eliminating variables in the process.

First, the temperature sweep test was executed from 170 to 250 °C since the range of temperature indicated for the commercial filament is between 180 and 215 °C. The results of the rheological tests revealed that the best temperature for processing each composite was identified in viscosity conditions close to those used commercially.

Figure 7 shows the storage modulus (*G′*) and loss modulus (*G″*) as a function of the temperature for the commercial and neat PLA. It was observed two different behaviors. In the temperature range indicated by the commercial filament, *G′* and *G″* values of neat PLA are lower than the commercial PLA. Beyond the polymer, commercial filaments usually have additives to tune the desired rheological properties for the FDM process or a molecular weight appropriated for this processing [49]. The neat PLA used here does not have any additional additives, and

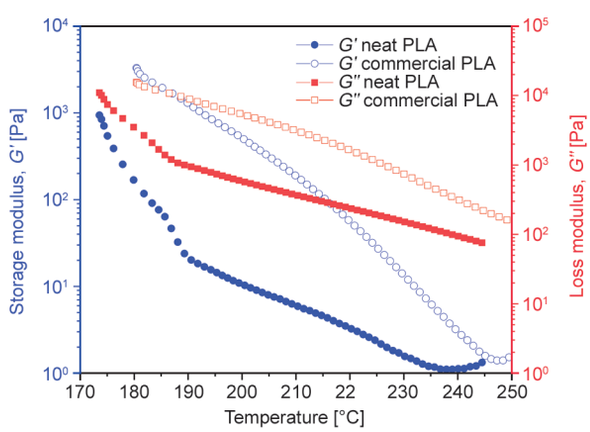

Figure 7. Rheological curves for commercial and pure PLA: *G″* and *G″ versus* temperature.

the molecular weight is probably not adequate for the FDM technique as filament. Consequently, the rheological properties do not match those of commercial ones. In FDM, the processing must occur so that the material presents good flow when flowing through the extruder nozzle and quickly solidifies when deposited [50]. So, the G'' (component linked to the viscous behavior of the material) of neat PLA must be approximately the same as G'' from commercial PLA. It is noted that neat PLA only resembles the commercial PLA in terms of G'' when subjected to lower temperatures, indicating that the process with neat PLA to be used by FDM must be carried out at lower temperatures when compared with the commercial PLA. For example, if the commercial PLA temperature is 210 °C, the adjustment of processing temperature of neat PLA must be 175 °C (according to match values of G'').

Figure 8 present the G'' and G', respectively, for commercial PLA and PLA/GO composites. Note that both G' and G'' did not show a similar behavior compared to commercial PLA, which difficulties the FDM processing. To achieve the desired behavior like the commercial PLA, the processing temperature reduction goes below the T_m of PLA, making its use in FDM processing unfeasible.

The G'' and G' curves for commercial PLA and PLA/HA/GO composites are also presented in Figure 8, respectively. Here, it is interesting to note that when HA is incorporated, the moduli approximate those verified in the commercial PLA, demonstrating an increase in flow resistance provided by HA, making the application of PLA/HA and PLA/HA/GO composites feasible in FDM processing.

Rheological tests of viscosity (η) *versus* shear rate ($\dot{\gamma}$) were performed for a more in-depth analysis of FDM processing issues. Figure 9 shows the curves for commercial and neat PLA, PLA/GO, and PLA/HA/GO composites. As with most thermoplastic materials, the PLA presents a Newtonian behavior until 10 s^{-1}; when increasing the shear rate, it becomes pseudoplastic, with a remarkable reduction in viscosity. Essential information can be verified that the insertion of GO led to lower viscosity values than neat PLA at the highest shear rates, inducing a lubrication process [51]. However, the neat PLA and all PLA/GO composites exhibited much lower viscosity than commercial PLA, proving the unfeasibility of using such materials in FDM processing. On the other hand, when HA is added to the PLA/GO composite, the values of viscosity are approached as exhibited by the commercial material. They showed similar behavior in the face of variations in the shear rate range analyzed.

Finally, the compilation of the rheological results demonstrated the feasibility of processing only in PLA/HA and PLA/HA/GO composites. Based on

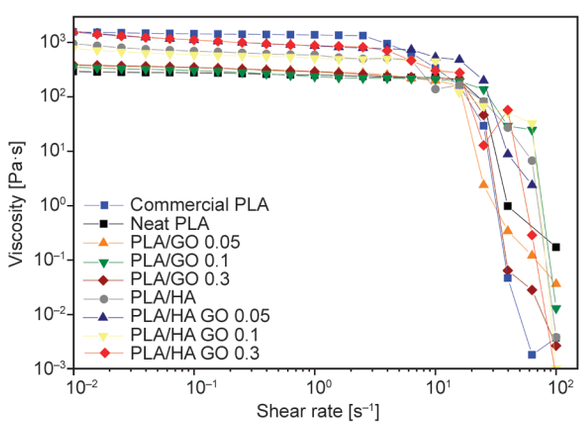

Figure 9. Viscosity *versus* shear rate for commercial and pure PLA, PLA/GO, PLA/HA and PLA/HA/GO composites.

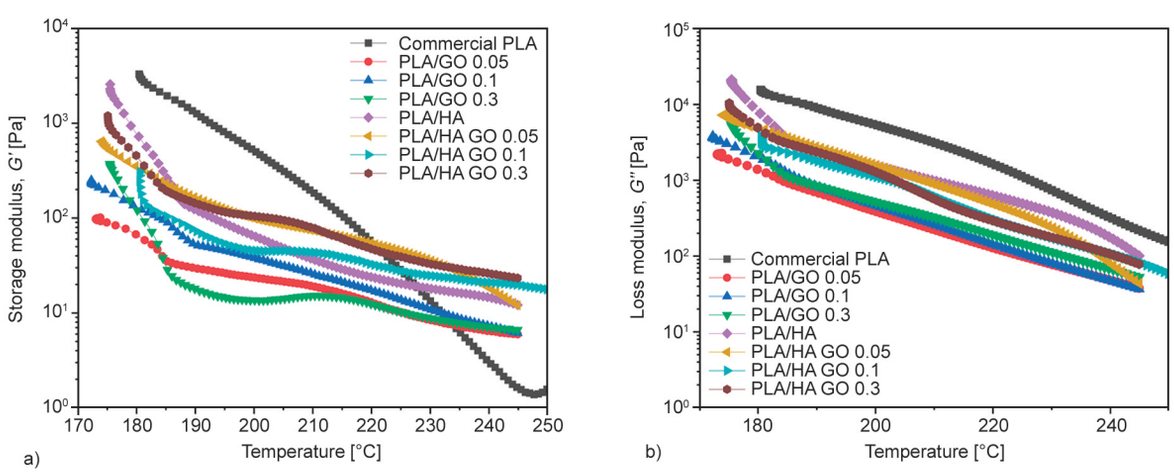

Figure 8. Storage (a) and loss (b) modulus for commercial PLA, PLA/GO, PLA/HA and PLA/HA/GO composites.

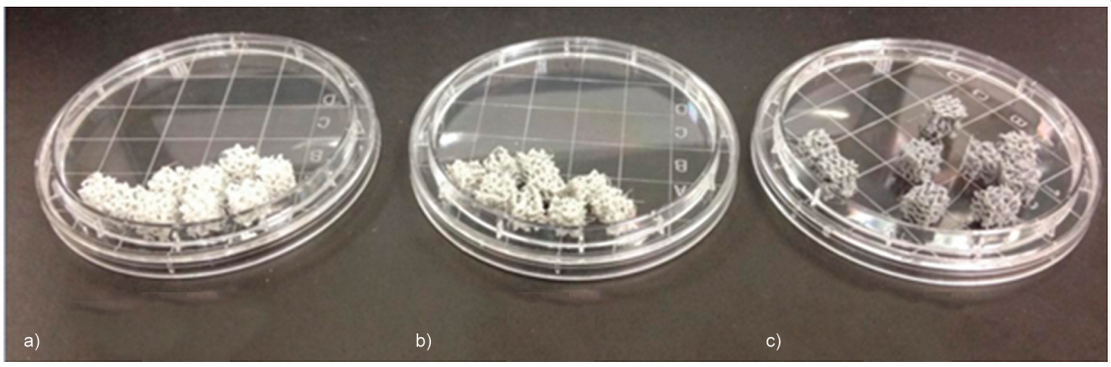

Figure 10. Scaffolds produced by FDM a) PLA/HA/GO 0.05, b) PLA/HA/GO 0.1 and c) PLA/HA/GO 0.3.

these results, FDM processing parameters were chosen for the samples. The temperature and the velocity processing were 174, 173 and 175 °C, and 100, 120 and 100%, for PLA/HA/GO 0.05, 0.1 and 0.3 wt%, respectively. Figure 10 shows the scaffolds produced by FDM for the PLA/HA/GO composites with 0.05, 0.1, and 0.3 wt.% of GO.

Cytocompatibility tests

The cell viability assay revealed that neither the scaffolds tested nor their extracts significantly decreased cell viability compared to the non-treated controls. Indeed, a mild reduction in cell viability could be observed with the scaffold containing 0.3% of GO. Still, this decrease was not high enough for the biomaterial to be considered cytotoxic (Table 6).

When the cell growth on top of the biomaterials was assessed, we observed that, although the scaffolds led to a lower proliferation compared to a surface that is industrially prepared for cell growth (the substrate of culture-treated 96 well plates), there was a significant growth of MC3T3 cell cells on the polymer scaffolds. The higher GO concentration led to a significantly lower cell proliferation than PLA scaffolds and over 30% lower than the 96 well plate substrate (Table 7).

These results were confirmed by the confocal images taken with cells seeded on top of PLA/HA discs with or without GO and compared to cells growing on glass cover slides (controls). The images (Figure 11 and Figure 12) show that the MC3T3 cells could adhere and grow successfully on the top of PLA discs (although at a lower rate than controls). Still, they were less able to multiply on top of PLA discs containing GO, especially with the highest concentration. Brightfield images from PLA/HA/GO discs were not taken as the materials were utterly opaque.

Table 6. Cell viability of MC3T3 cell in the presence of PLA/HA scaffolds with GO and their extracts in culture media.

Sample	Cell viability [%]		
	24 h	48 h	1 week
PLA/HA/GO 0.05	103.48±9.06	100.16±5.78	97.48±6.63
PLA/HA/GO 0.3	88.14±4.56	85.79±3.31	84.64±4.16
Extract PLA/HA/GO 0.05	106.30±13.35	90.63±10.47	103.48±9.06
Extract PLA/HA/GO 0.3	109.01±9.63	93.13±2.60	88.14±4.56
Control +	8.34±0.35	7.81±0.36	8.34±0.35
Control –	100.00±7.04	100.00±11.72	100.00±7.04

Table 7. Percentage of MC3T3 cell proliferation on top of the PLA/HA/GO discs compared to their proliferation in 96-well plate substrates.

Sample	Cell proliferation [% of control]
PLA*	74.63±4.69
PLA/HA/GO 0.05	68.90±2.78
PLA/HA/GO 0.3*	66.89±2.07
Control cells	100.00±5.42

*Statistically significant difference with control ($p < 0.05$)

4. Conclusions

The production of a filament based on PLA as a polymeric matrix and GO and HA as filler was carried out to prepare scaffolds for tissue engineering. For this goal, first, the GO was synthesized, and the results obtained by Raman, XRD, and TGA confirmed the oxidative process of graphite, producing graphite oxide (GrO), the precursor of GO. From DSC results, the GO alone did not act as nucleating for PLA crystal growth. However, the incorporation of HA in the matrix led to an increase in the crystallinity degree. The composite with lower GO content (0.05 wt%) achieved the best results regarding

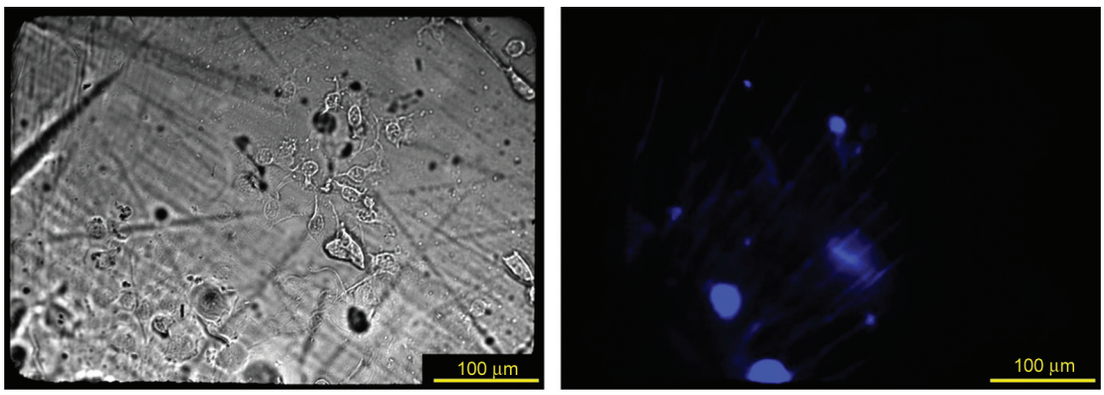

Figure 11. Confocal images of cells growing on PLA scaffolds (without hydroxyapatite of graphene oxide) a) the brightfield image, and b) the DAPI fluorescence image.

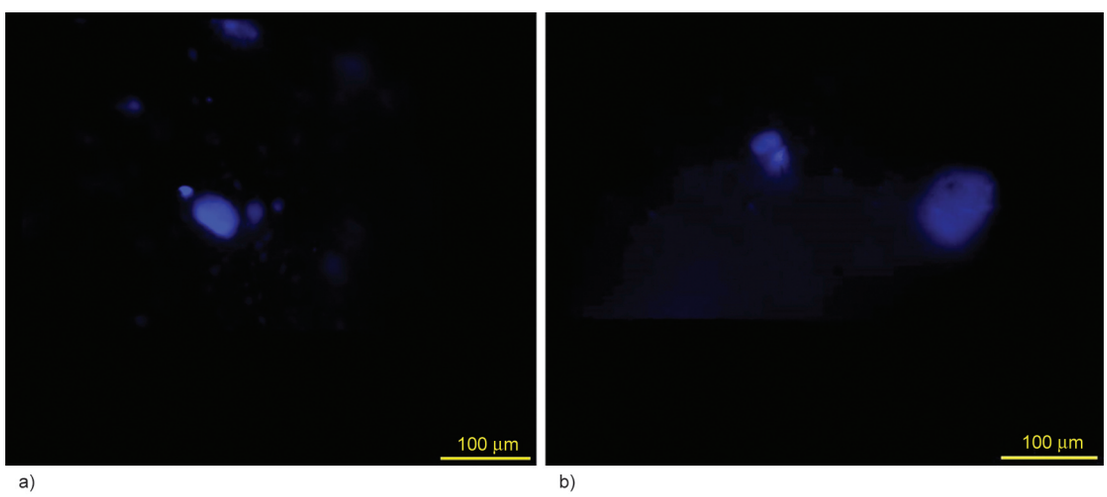

Figure 12. Confocal images of cells growing on PLA/HA/GO scaffolds a) the DAPI fluorescence image of PLA/HA/GO 0.05, and b) the DAPI fluorescence image of PLA/HA/GO 0.3.

mechanical properties, mainly due to the production process of composites via melt mixing, which probably led to good filler distribution and dispersion in addition to a good filler/matrix interface interaction. Regarding cytocompatibility, PLA/HA/GO 0.05 was also the best option, as the cell viability remains close to the control cells, and the cell proliferation is more intense than the PLA/HA/GO with 0.3% of GO. Even at low concentrations, GO facilitates processing in the 3D printer. However, the rheological parameters must always be adjusted to produce parts with quality compared to commercial PLA. GO's properties are promising, and it can extend the range of applications of PLA/HA-based biomaterials.

It is essential to point out that mechanical properties improvements can affect scaffolds' degradation rate in a biological environment by influencing degradation mechanisms, enhancing biocompatibility, and providing mechanical stability. Balancing these factors is essential to designing scaffolds that support tissue regeneration effectively while maintaining structural integrity during degradation.

Acknowledgements

The authors would like to acknowledge FAPESP – Fundação de Amparo à Pesquisa do Estado de São Paulo (Process 2022/07054-8 and 2020/14302-2), CNPq – Conselho Nacional de Desenvolvimento Científico e Tecnológico (Process 314093/2021-4 and 408798/2022-0) for funding this work.

References

[1] Prasad A.: State of art review on bioabsorbable polymeric scaffolds for bone tissue engineering. Materials Today: Proceedings, **44**, 1391–1400 (2021). https://doi.org/10.1016/j.matpr.2020.11.622

[2] Kalsi S., Singh J., Sehgal S. S., Sharma N. K.: Biomaterials for tissue engineered bone scaffolds: A review. Materials Today: Proceedings, **81**, 888–893 (2023). https://doi.org/10.1016/j.matpr.2021.04.273

[3] Kumar M., Sharma V.: Additive manufacturing techniques for the fabrication of tissue engineering scaffolds: A review. Rapid Prototyping Journal, **27**, 1230–1272 (2021).
https://doi.org/10.1108/RPJ-01-2021-0011

[4] Korpela J., Kokkari A., Korhonen H., Malin M., Närhi T., Seppäleä J.: Biodegradable and bioactive porous scaffold structures prepared using fused deposition modeling. Journal of Biomedical Materials Research Part B: Applied Biomaterials, **101**, 610–619 (2013).
https://doi.org/10.1002/jbm.b.32863

[5] Winarso R., Anggoro P. W., Ismail R., Jamari J., Bayuseno A. P.: Application of fused deposition modeling (FDM) on bone scaffold manufacturing process: A review. Heliyon, **8**, e11701 (2022).
https://doi.org/10.1016/j.heliyon.2022.e11701

[6] Kim C. G., Han K. S., Lee S., Kim M. C., Kim S. Y., Nah J.: Fabrication of biocompatible polycaprolactone–hydroxyapatite composite filaments for the FDM 3D printing of bone scaffolds. Applied Sciences, **11**, 6351 (2021).
https://doi.org/10.3390/app11146351

[7] Camargo J. C., Machado Á. R., Almeida E. C., Silva E. F. M. S.: Mechanical properties of PLA-graphene filament for FDM 3D printing. International Journal of Advanced Manufacturing Technology, **103**, 2423–2443 (2019).
https://doi.org/10.1007/s00170-019-03532-5

[8] Corcione C. E., Gervaso F., Scalera F., Padmanabhan S. K., Madaghiele M., Montagna F., Sannino A., Licciulli A., Maffezzoli A.: Highly loaded hydroxyapatite microsphere/PLA porous scaffolds obtained by fused deposition modelling. Ceramics International, **45**, 2803–2810 (2019).
https://doi.org/10.1016/j.ceramint.2018.07.297

[9] Kovalcik A., Sangroniz L., Kalina M., Skopalova K., Humpolíček P., Omastova M., Mundigler N., Müller A. J.: Properties of scaffolds prepared by fused deposition modeling of poly(hydroxyalkanoates). International Journal of Biological Macromolecules, **161**, 364–376 (2020).
https://doi.org/10.1016/j.ijbiomac.2020.06.022

[10] Kosorn W., Wutticharoenmongkol P.: Poly(ε-caprolactone)/poly(3-hydroxybutyrate-*co*-3-hydroxyvalerate) blend from fused deposition modeling as potential cartilage scaffolds. International Journal of Polymer Science, **2021**, 6689789 (2021).
https://doi.org/10.1155/2021/6689789

[11] Singhvi M. S., Zinjarde S. S., Gokhale D. V.: Polylactic acid: Synthesis and biomedical applications. Journal of Applied Microbiology, **127**, 1612–1626 (2019).
https://doi.org/10.1111/jam.14290

[12] DeStefano V., Khan S., Tabada A.: Applications of PLA in modern medicine. Engineered Regeneration, **1**, 76–87 (2020).
https://doi.org/10.1016/j.engreg.2020.08.002

[13] Ramesh N., Moratti S. C., Dias G. J.: Hydroxyapatite–polymer biocomposites for bone regeneration: A review of current trends. Journal of Biomedical Materials Research Part B: Applied Biomaterials, **106**, 2046–2057 (2018).
https://doi.org/10.1002/jbm.b.33950

[14] Zhang B., Wang L., Song P., Pei X., Sun H., Wu L., Zhou C., Wang K., Fan Y., Zhang X.: 3D printed bone tissue regenerative PLA/HA scaffolds with comprehensive performance optimizations. Materials and Design, **201**, 109490 (2021).
https://doi.org/10.1016/j.matdes.2021.109490

[15] Backes E. H., de Nóbile Pires L., Beatrice C. A. G., Costa L. C., Passador F. R., Pessan L. A.: Fabrication of biocompatible composites of poly(lactic acid)/hydroxyapatite envisioning medical applications. Polymer Engineering and Science, **60**, 636–644 (2020).
https://doi.org/10.1002/pen.25322

[16] Zare R. N., Doustkhah E., Assadi M. H. N.: Three-dimensional bone printing using hydroxyapatite-PLA composite. Materials Today: Proceedings, **42**, 1531–1533 (2019).
https://doi.org/10.1016/j.matpr.2019.12.046

[17] Pandele A. M., Constantinescu A., Radu I. C., Miculescu F., Voicu S. I., Ciocan L. T.: Synthesis and characterization of PLA-micro-structured hydroxyapatite composite films. Materials, **13**, 274 (2020).
https://doi.org/10.3390/ma13020274

[18] Bernardo M. P., da Silva B. C. R., Hamouda A. E. I., de Toledo M. A. S., Schalla C., Rütten S., Goetzke R., Mattoso L. H. C., Zenke M., Sechi A.: PLA/hydroxyapatite scaffolds exhibit *in vitro* immunological inertness and promote robust osteogenic differentiation of human mesenchymal stem cells without osteogenic stimuli. Scientific Reports, **12**, 2333 (2022).
https://doi.org/10.1038/s41598-022-05207-w

[19] Gruber P., Ziółkowski G., Gazińska M., Kryszak B., Krokos A., Olejarczyk M., Szymczyk-Ziółkowska P., Dzienny P., Antończak A. J.: High porosity composite structures produced from poly(lactic acid)/hydroxyapatite microspheres using novel dual beam laser sintering method: Analysis of structural, mechanical and thermal properties. Journal of Manufacturing Processes, **84**, 1284–1297 (2022)
https://doi.org/10.1016/j.jmapro.2022.11.010

[20] Sreenivasulu B., Ramji B. R., Nagaral M.: A review on graphene reinforced polymer matrix composites. Materials Today: Proceedings, **5**, 2419–2428 (2018).
https://doi.org/10.1016/j.matpr.2017.11.021

[21] Pinto G. M., Cremonezzi J. M. O., Ribeiro H., Andrade R. J. E., Demarquette N. R., Fechine G. J. M.: From two-dimensional materials to polymer nanocomposites with emerging multifunctional applications: A critical review. Polymer Composites, **44**, 1438–1470 (2023).
https://doi.org/10.1002/pc.27213

[22] Zare P., Aleemardani M., Seifalian A., Bagher Z., Seifalian A. M.: Graphene oxide: Opportunities and challenges in biomedicine. Nanomaterials, **11**, 1083 (2021). https://doi.org/10.3390/nano11051083

[23] Priyadarsini S., Mohanty S., Mukherjee S., Basu S., Mishra M.: Graphene and graphene oxide as nanomaterials for medicine and biology application. Journal of Nanostructure in Chemistry, **8**, 123–137 (2018). https://doi.org/10.1007/s40097-018-0265-6

[24] Gong M., Zhao Q., Dai L., Li Y., Jiang T.: Fabrication of polylactic acid/hydroxyapatite/graphene oxide composite and their thermal stability, hydrophobic and mechanical properties. Journal of Asian Ceramic Societies, **5**, 160–168 (2017). https://doi.org/10.1016/j.jascer.2017.04.001

[25] Ma H. B., Su W. X., Tai Z. X., Sun D. F., Yan X. B., Liu B., Xue Q. J.: Preparation and cytocompatibility of polylactic acid/hydroxyapatite/graphene oxide nanocomposite fibrous membrane. Chinese Science Bulletin, **57**, 3051–3058 (2012). https://doi.org/10.1007/s11434-012-5336-3

[26] Liu S., Wu X., Hu J., Wu Z., Zheng Y.: Preparation and characterisation of a novel polylactic acid/hydroxyapatite/graphene oxide/aspirin drug-loaded biomimetic composite scaffold. New Journal of Chemistry, **45**, 10788–10797 (2021). https://doi.org/10.1039/d1nj01045j

[27] Medeiros G. S., Muñoz P. A. R., de Oliveira C. F. P., da Silva L. C. E., Malhotra R., Gonçalves M. C., Rosa V., Fechine G. J. M.: Polymer nanocomposites based on poly(ε-caprolactone), hydroxyapatite and graphene oxide. Journal of Polymers and the Environment, **28**, 331–342 (2020). https://doi.org/10.1007/s10924-019-01613-w

[28] Muñoz P. A. R., de Oliveira C. F. P., Amurin L. G., Rodriguez C. L. C., Nagaoka D. A., Tavares M. I. B., Domingues S. H., Andrade R. J. E., Fechine G. J. M.: Novel improvement in processing of polymer nanocomposite based on 2D materials as fillers. Express Polymer Letters, **12**, 930–945 (2018). https://doi.org/10.3144/expresspolymlett.2018.79

[29] Ferri J. M., Jordá J., Montanes N., Fenollar O., Balart R.: Manufacturing and characterization of poly(lactic acid) composites with hydroxyapatite. Journal of Thermoplastic Composite Materials, **31**, 865–881 (2018). https://doi.org/10.1177/0892705717729014

[30] Shimizu R. N., Demarquette N. R.: Evaluation of surface energy of solid polymers using different models. Journal of Applied Polymer Science, **76**, 1831–1845 (2000). https://doi.org/10.1002/(SICI)1097-4628(20000620)76:12<1831::AID-APP14>3.0.CO;2-Q

[31] Garlotta D.: A literature review of poly(lactic acid). Journal of Polymers and the Environment, **9**, 63–84 (2019). https://doi.org/10.1023/A:1020200822435

[32] Su C-Y., Xu Y., Zhang W., Zhao J., Tang X., Tsai C-H., Li L-J.: Electrical and spectroscopic characterizations of ultra-large reduced graphene oxide monolayers. Chemistry of Materials, **21**, 5674–5680 (2009). https://doi.org/10.1021/cm902182y

[33] Perrozzi F., Prezioso S., Ottaviano L.: Graphene oxide: From fundamentals to applications. Journal of Physics Condensed Matter, **27**, 013002 (2015). https://doi.org/10.1088/0953-8984/27/1/013002

[34] Araujo P. T., Terrones M., Dresselhaus M. S.: Defects and impurities in graphene-like materials. Materials Today, **15**, 98–109 (2012). https://doi.org/10.1016/S1369-7021(12)70045-7

[35] Li H., Zhu Y., Mao Z., Gu J., Zhang J., Qian Y.: Synthesis and characterization of carbon fibrils formed by stacking graphite sheets of nanometer thickness. Carbon, **47**, 328–330 (2009). https://doi.org/10.1016/j.carbon.2008.09.053

[36] Zhao W., Kido G., Hara K., Noguchi H.: Characterization of neutralized graphite oxide and its use in electric double layer capacitors. Journal of Electroanalytical Chemistry, **712**, 185–193 (2014). https://doi.org/10.1016/j.jelechem.2013.11.007

[37] Song J., Wang X., Chang C-T.: Preparation and characterization of graphene oxide. Journal of Nanomaterials, **2014**, 276143 (2014). https://doi.org/10.1155/2014/276143

[38] Kamalanathan P., Ramesh S., Bang L. T., Niakan A., Tan C. Y., Purbolaksono J., Chandran H., Teng W. D.: Synthesis and sintering of hydroxyapatite derived from eggshells as a calcium precursor. Ceramics International, **40**, 16349–16359 (2014). https://doi.org/10.1016/j.ceramint.2014.07.074

[39] Guillen-Romero L. D., Oropeza-Guzmán M. T., López-Maldonado E. A., Iglesias A. L., Paz-González J. A., Ng T., Serena-Gómez E., Villarreal-Gómez L. J.: Synthetic hydroxyapatite and its use in bioactive coatings. Journal of Applied Biomaterials and Functional Materials, **17**, 1–12 (2019). https://doi.org/10.1177/2280800018817463

[40] Surekha G., Krishnaiah K. V., Ravi N., Suvarna R. P.: FTIR, Raman and XRD analysis of graphene oxide films prepared by modified Hummers method. Journal of Physics: Conference Series, **1495**, 012012 (2020). https://doi.org/10.1088/1742-6596/1495/1/012012

[41] Zheng Y., Xiong C., Wang Z., Zhang L.: Enhanced osteoblast cells adhesion, spreading, and proliferation to surface-carboxylated poly(etheretherketone). Journal of Bioactive and Compatible Polymers, **30**, 302–318 (2015). https://doi.org/10.1177/0883911515572494

[42] Gentleman M. M., Gentleman E.: The role of surface free energy in osteoblast-biomaterial interactions. International Materials Reviews, **59**, 417–429 (2014). https://doi.org/10.1179/1743280414Y.0000000038

[43] Tham C. Y., Hamid Z. A. A., Ahmad Z., Ismail H.: Surface modification of poly(lactic acid) (PLA) *via* alkaline hydrolysis degradation. Advanced Materials Research, **970**, 324–327 (2014). https://doi.org/10.4028/www.scientific.net/AMR.970.324

[44] Grenho L., Manso M. C., Monteiro F. J., Ferraz M. P.: Adhesion of *Staphylococcus aureus*, *Staphylococcus epidermidis*, and *Pseudomonas aeruginosa* onto nanohydroxyapatite as a bone regeneration material. Journal of Biomedical Materials Research: Part A, 100A, 1823–1830 (2012). https://doi.org/10.1002/jbm.a.34139

[45] Dimiev A. M., Eigler S.: Graphene oxide: Fundamentals and applications. Wiley, New Jersey (2016).

[46] Sadi R. K., Fechine G. J. M., Demarquette N. R.: Photodegradation of poly(3-hydroxybutyrate). Polymer Degradation and Stability, **95**, 2318–2327 (2010). https://doi.org/10.1016/j.polymdegradstab.2010.09.003

[47] Baradaran S., Moghaddam E., Basirun W. J., Mehrali M., Sookhakian M., Hamdi M., Moghaddam M. R. N., Alias Y.: Mechanical properties and biomedical applications of a nanotube hydroxyapatite-reduced graphene oxide composite. Carbon, **69**, 32–45 (2014). https://doi.org/10.1016/j.carbon.2013.11.054

[48] Harper E. J.: Bioactive bone cements. Proceedings of the Institution of Mechanical Engineers Part H: Journal of Engineering in Medicine, **212**, 113–120 (1998). https://doi.org/10.1243/0954411981533881

[49] Arrigo R., Frache A.: FDM printability of PLA based-materials: The key role of the rheological behavior. Polymers, **14**, 1754 (2022). https://doi.org/10.3390/polym14091754

[50] Gibson I., Rosen D., Stucker B.: Additive manufacturing technologies: 3D printing, rapid prototyping, and direct digital manufacturing. S pringer, New York (2015).

[51] Ferreira E. H. C., Andrade R. J. E., Fechine G. J. M.: The “superlubricity state” of carbonaceous fillers on polyethylene-based composites in a molten state. Macromolecules, **52**, 9620–9631 (2019). https://doi.org/10.1021/acs.macromol.9b01746